Applied Catalysis B: Environmental 277 (2020) 119241

Contents lists available at ScienceDirect

Applied Catalysis B: Environmental

journal homepage: www.elsevier.com/locate/apcatb

Highly stable two-dimensional bismuth metal-organic frameworks for efficient electrochemical reduction of CO_2

Fang Li[a], Geun Ho Gu[b], Changhyeok Choi[b], Praveen Kolla[c,*], Song Hong[d], Tai-Sing Wu[e], Yun-Liang Soo[e], Justus Masa[f], Sanjeev Mukerjee[c], Yousung Jung[b,*], Jieshan Qiu[g], Zhenyu Sun[a,*]

[a] State Key Laboratory of Organic-Inorganic Composites, College of Chemical Engineering, Beijing University of Chemical Technology, Beijing, 100029, PR China
[b] Department of Chemical and Biomolecular Engineering, Korea Advanced Institute of Science and Technology (KAIST), Daejeon, 34141, Republic of Korea
[c] Northeastern University Center for Renewable Energy Technology, Department of Chemistry and Chemical Biology, Northeastern University, 317 Egan Research Center, 360 Huntington Avenue, Boston, Massachusetts, 02115, United States
[d] Analysis Technology R&D Center, Beijing University of Chemical Technology, Beijing, 100029, PR China
[e] Department of Physics, National Tsing Hua University, Hsinchu, 30013, Taiwan
[f] Analytische Chemie-Elektroanalytik & Sensorik, Ruhr University Bochum, D-44780, Bochum, Germany
[g] State Key Laboratory of Chemical Resource Engineering, College of Chemical Engineering, Beijing University of Chemical Technology, Beijing, 100029, PR China

ARTICLE INFO

Keywords:
CO_2 reduction
Electrocatalyis
Metal-organic framwork
Bismuth
Formic acid

ABSTRACT

We report a unique 2D bismuth metal-organic framework (Bi-MOF) that possesses permanent accessible porosity for efficient electrochemical CO_2 reduction (ECR) to HCOOH. The 2D open-framework structure with helical Bi-O rods bridged by tritopic carboxylate ligands exhibits a remarkable Faradaic efficiency for HCOOH formation over a broad potential window, reaching 92.2 % at ~ –0.9 V (*vs.* reversible hydrogen electrode, RHE) with excellent durability over 30 h. The mass-specific HCOOH partial current density is up to 41.0 mA mg_{Bi}^{-1}, exceeding 4 times higher than that of commercial Bi_2O_3 and Bi sheets at ~ –1.1 V (*vs.* RHE). Operando and *ex-situ* X-ray absorption fine structure spectroscopy revealed a structural feature associated with Bi-MOF to preserve Bi (3+) during and after long-term ECR. Theoretical calculations further showed that the crystallographically channels with abundant Bi active sites in the MOF structure favor the formation of *HCOO while suppressing the side-reaction of hydrogen evolution, thereby leading to the high selectivity for HCOOH.

1. Introduction

Electrochemical CO_2 reduction (ECR), powered by renewable electricity, offers a promising approach to convert undesirable and cost-free CO_2 into fuels and commodity chemicals [1–8]. This prospect can also address storage issues for intermittent energy resources, thereby enabling a carbon-neutral energy cycle. However, CO_2 is thermodynamically very stable, which necessitates high electrical energy input and poses further challenges associated with reaction selectively to convert CO_2 into a specific product of interest. In addition, nucleophilic attack at least one of the C atoms is required to bend the linear O=C=O bond [9–11]. Moreover, promotion of simultaneous transfer of electrons and protons in pairs is essential to obviate the formation of $CO_2^{\cdot -}$ and promote CO_2 reduction. Furthermore, stabilizing the intermediates of CO_2 reduction could potentially limit the number of transitions involving electron and proton transitions [12,13]. Among the value-added products, formic acid (HCOOH) holds promise as a hydrogen energy carrier and feedstock for direct-HCOOH fuel cells. Great efforts have been attempted to screen and design materials for the electrocatalytic reduction of CO_2 to $HCOOH/HCOO^-$ [14–17], however, the development of active, selective, stable yet cheap electrocatalysts that are naturally abundant remains an ongoing challenge for wide commercialization of this technology.

Sp post-transition metals with a d^{10} electronic configuration such as Pd, In, Sn, Hg, and Pb have been demonstrated to favour the formation of $HCOOH/HCOO^-$ owing to their weak adsorption capacities for $CO_2^{\cdot -}$ [18,19]. However, the conversion rate and stability of the most electrocatalysts reported thus far are not viable [20,21]. Bismuth (Bi) is regarded as an attractive metal for ECR because of its cost-effectiveness, earth-abundance, nontoxicity, and low activity for the hydrogen evolution reaction (HER) that is the competing reaction during ECR at cathodic-potentials. Nanostructuring of Bi to form nanosheets [22], single sites [23], and nanocomposites [24–27] has been shown to enhance ECR by providing more exposed surface active sites than their

* Corresponding authors.
E-mail addresses: drpraveenkolla@gmail.com (P. Kolla), ysjn@kaist.ac.kr (Y. Jung), sunzy@mail.buct.edu.cn (Z. Sun).

https://doi.org/10.1016/j.apcatb.2020.119241
Received 17 April 2020; Received in revised form 31 May 2020; Accepted 13 June 2020
Available online 15 June 2020
0926-3373/

bulk counterparts. Especially, the metal-organic frameworks (MOFs) with unsaturated metal sites show a potential in trapping CO_2, thus facilitating concentrated CO_2 at the electrode surface, which is further beneficial for overcoming mass transfer limitation due to low CO_2 solubility and improving the electrochemical CO_2 conversion turnover frequency [28–31]. The linker species in the MOF structure can also modify the adsorption behaviours of water and CO_2 reduction intermediates, providing the opportunity for fine-tuning the ECR selectivity. Nevertheless, there are very few reports on the application of MOFs in ECR and therefore deserves a through exploration of Bi-based MOF. Herein, we report highly efficient ECR to produce HCOOH over a helical rod-based Bi-MOF with crystallographically independent channels, affording a Faradaic efficiency (*FE*) of up to 92.2 % at an applied potential of ~ –0.9 V (*vs*. -RHE) under ambient conditions. The *FE* for HCOOH formation was over 85.0 % through a wide range of potentials from ~ –0.8 to ~ –1.1 V (*vs*. RHE). However, the HCOOH partial current density increased with overpotential, reaching 15.0 mA cm^{-2} at ~ –1.1 V (*vs*. RHE). Moreover, HCOOH partial current densities were also found to be dependent on the type of electrolyte medium, which proportionally increased with electrolyte pH while maintaining consistent HCOOH *FE*s of above 90.0 %. The highest HCOOH partial current density (of 14.0 mA cm^{-2}) was observed at a low overvoltage of 0.61 V in 1 M KOH solution. The electronic structure evolution of Bi in the MOF structure during and after ECR is further studied using *in-situ* and *ex-situ* X-ray absorption fine structure spectroscopy, respectively. Furthermore, density functional theory (DFT) calculations provide an insight into the reaction pathways and key intermediates responsible for the high ECR activity and HCOOH selectivity of the Bi-MOF.

2. Experimental

2.1. Reagents and materials

All chemicals used in this work were of analytical grade and used without further treatments. Anhydrous methanol, isopropanol (IPA), 1,3,5-benzenetricarboxylic acid (H_3BTC), Bi powder, terephthalic acid (TPA), 2-aminoterephthalic acid (ATPA), N, N-dimethylformamide (DMF), acetonitrile (MeCN), and 2,5-dichloroterephthalic acid (DCTPA) were obtained from Aladdin. Bismuth nitrate pentahydrate ($Bi(NO_3)_3{\cdot}5H_2O$), 1,3,5-tri (4-carboxyphenyl) benzene (H_3BTB), biphenyl-3,3',5,5'-tetracarboxylic acid, and bulk Bi_2O_3 were purchased from Macklin. Carbon black was provided by Beijing Chemical Reagent Company. Nafion solution (5.0 wt%) was supplied by Sigma-Aldrich and Nafion membranes were provided by Alfa Aesar. Deionized water (18.2 megohm·cm) was obtained from a Millipore system. Carbon dioxide gas (99.999 % purity) and argon gas (99.999 % purity) were both provided by Beijing Haipu Gas Company. Ltd.

2.2. Preparation of Bi-MOF (CAU-17)

150 mg of $Bi(NO_3)_3{\cdot}5H_2O$ and 750 mg of H_3BTC were added into 60 mL of anhydrous methanol in a round-bottom flask at room temperature under magnetically stirring for 30 min. The homogeneous mixture was then transferred into a Teflon-lined steel reactor (100 mL) which was sealed and heated at 120 °C for 24 h. The resulting white powder was collected by filtration and washed with methanol. After drying in an oven at 60 °C for 3 h, the final product was obtained.

2.3. Characterization

X-ray powder diffraction (XRD) was performed with a D/MAX-RC diffractometer operated at 30 kV and 100 mA with Cu-Kα radiation. XPS experiments were carried out using Thermo Scientific ESCALAB 250Xi instrument. The instrument was equipped with an electron flood and scanning ion gun. All spectra were calibrated to the C 1s binding energy at 284.8 eV. Scanning electron microscopy (SEM) was carried out using a field emission microscope (JEOL JSM-7800F) operated at 5 kV. High-angle annular dark-field scanning TEM (HAADF-STEM) was conducted using a JEOL ARM200 microscope with 200 kV accelerating voltage. STEM samples were prepared by depositing a droplet of suspension onto a Cu grid coated with a Lacey Carbon film. Nitrogen adsorption/desorption measurements at 77 K were performed on a Micromeritics ASAP2460 to obtain pore properties such as the specific surface area, total pore volume, and pore size distribution. The sample was degassed at 180 °C for 10 h.

X-ray absorption fine structure (XAFS) of Bi-MOF catalyst was studied in a home-made three-electrode cell that was specifically designed for XAS analysis. This *in-situ* cell comprises of Bi-MOF (with catalyst loading of 1 mg/cm^2) as working electrode (WE) while carbon electrode and reversible hydrogen electrode (RHE) were used as counter and reference electrodes, respectively. The cell is also designed to allow direct-exposure of X-ray beam onto Bi-MOF catalyst (WE) through a transparent Kapton® window that was affixed at the beam-slit to contain liquid electrolyte. The cell was placed at 45° to the incoming X-ray beam for collecting XAS spectra in both fluorescent and transmission modes without interfering with other cell components and liquid electrolyte.

CO_2 pre-saturated 0.1 M $KHCO_3$ electrolyte (flow rate 5 mL/min) was used for *in-situ* electrochemical measurements while a constant CO_2-bubbling was maintained (20 sccm of CO_2 gas) in the external electrolyte reservoir. Bi L-3 fluorescence data were collected by a Vortex ME4 detector using the fluorescence mode. Before each In-situ electrochemical XAS measurement, samples were kept at desired potentials for 15 min in order to reach interfacial-equilibrium and steady-state conditions. The *ex-situ* XAS measurements of before and after electrolyzed catalyst powders were collected in transmission mode. Data reduction and analysis were performed using Athena and Artemis software. The *in-situ* studies were conducted for extended X-ray absorption structure (EXAFS) fitting, Bi and Bi_2O_3 standards were used to obtain the amplitude reduction factor (σ_0^2) values, which were further used to calculated other fitting parameters.

2.4. Electrochemical measurements

Typically, 10 mg of a catalyst was dispersed in 2 mL of a solution containing isopropanol, deionized water, and Nafion solution (5.0 wt%) with a corresponding volume ratio of 100: 100: 1 under bath ultrasonication for 30 min to form a homogeneous ink. 200 μL of the dispersion was then loaded onto a carbon paper electrode with a size of 1cm × 1cm, which was then dried under ambient conditions. For linear sweep voltammograms in Ar- or CO_2-saturated 0.1 M $KHCO_3$ solution, 6 mg of a catalyst was dispersed in a mixture of ethanol (600 μL), deionized water (600 μL), and Nafion solution (5.0 wt%, 600 μL). Subsequently, the mixture was ultrasonicated for 30 min to form a homogeneous ink. 7.95 μL of the dispersion was then deposited onto a glassy carbon electrode and dried under ambient conditions.

Controlled potential electrolysis of CO_2 was tested in an H-cell system, which was separated by a Nafion 117 membrane. Before ECR tests, the Nafion membrane was pre-treated by heating in H_2O_2 aqueous solution (5.0 %) and H_2SO_4 (0.5 M) at 80 °C for 1 h, respectively. Then the Nafion membrane was immersed in deionized water under ambient conditions for 30 min and then washed with deionized water. Toray Carbon fiber paper with a size of 1 cm × 1 cm was used as working electrode. Pt wire and Ag/AgCl electrodes were used as counter electrode and reference electrode, respectively. The potentials were controlled by an electrochemical working station (CHI 760E, Shanghai CH Instruments Co., China). Unless otherwise stated, all the potentials were iR-corrected by E (correction) = E (test) – I (test) × R_s. All potentials in this study were measured against the Ag/AgCl reference electrode (in KCl solution, 3.5 M) and converted to the RHE reference scale by

$$E\ (vs.\ \text{RHE}) = E\ (vs.\ \text{Ag/AgCl}) + 0.197 + 0.0591 \times \text{pH} \quad (1)$$

Electrocatalytic CO_2 reduction was conducted in CO_2-saturated $KHCO_3$ solution (0.1 M) at room temperature and atmospheric pressure. CO_2 was purged into the $KHCO_3$ solution for at least 30 min to remove residual air in the reservoir, then controlled potential electrolysis was performed at each potential for 60 min.

Linear sweep voltammograms in Ar- or CO_2 atmosphere were carried out in a three-electrode system using Ag/AgCl as reference electrode, Pt wire as counter electrode, and glassy carbon as working electrode on a CHI 760E potentiostat. Rotating disk electrode (RDE) experiments were run on an AFMSRCE RDE control system (Pine Inc., USA). The electrolyte is 0.1 M $KHCO_3$ solution purged with Ar or CO_2 over 30 min.

2.5. Quantitative analysis of gaseous and liquid products

The gas-phase product analysis for the electrochemical experiments was carried out using an Agilent 7890B gas chromatography (GC) system with two thermal conductivity detectors (TCD) and one flame ionization detector (FID). To characterize the gas product, 20 mL of produced gas in the dead volume of a gas bag (~ 2 L) was injected into the GC at identical experimental conditions (e.g., pressure, temperature, and time) using sample lock syringe. CO and H_2 mole fractions of injected samples were calculated using GC calibration curve. After electrolysis process, electrolyte was collected to quantificationally analyze the amounts of liquid products (n in moles) by nuclear magnetic resonance (NMR, Bruker Avance III 400 HD spectrometer). NMR samples were prepared by mixing 0.5 mL of the product-containing electrolyte and 0.1 mL DMSO-d_6 as the internal standard. The concentration of formic acid was determined by the standard curve using various concentrations (0.5, 1.0, 2.0, 5.0, and 10.0 mM) of formic acid and the internal standard. The linear relationship between the known formic acid concentration and relative area (*vs*. DMSO) was made into a standard curve (as shown in Supporting Information). The *FE* of products can be calculated via the following equation:

$$FE = Q_{HCOOH} / Q_{total} = (mF \times n) / (I \times t) \quad (2)$$

Where F is the Faraday constant (96,485 C mol^{-1}), n the number of moles for a given product, m (in number) the required electrons for the generation of one product molecule (e.g., formic acid, CO, H_2 or hydrocarbons, etc.). The amount of charge (Q in Coulomb) passed to produce products during a period of reaction time was calculated. I (in ampere) is the constant current at an applied potential and t (in second) is the time consumed at the corresponding current during the electrolysis process.

$$EE = FE(\%) \times \Delta E^0_{HCOOH} / \Delta E_{HCOOH} \quad (3)$$

Where *EE* is the energetic efficiency, ΔE^0_{HCOOH} represents the difference between the reference voltage for H_2O oxidation and $CO_2-HCOOH$ reduction, and ΔE_{HCOOH} corresponds to the difference between the reference voltage for H_2O oxidation and the applied potential over catalyst.

3. Results and discussion

3.1. Morphology and microstructure

We used a facile one-step solvothermal method to prepare Bi-MOFs with tunable crystallinity and coordination environments via manipulation of reaction temperature and organic linker types. Fig. 1a shows the crystal structure of a Bi-MOF (CAU-17) constructed of tritopic linkers (1,3,5-benzenetricarboxylic acid, H_3BTC). The XRD pattern of the as-synthesized sample is given in Fig. 1b, showing typical diffraction peaks of CAU-17, reasonably consistent with the theoretical results [32,33], confirming the formation of a crystalline open-framework structure. The wide-scan X-ray photoelectron spectroscopy (XPS) survey spectrum indicates the spectroscopic features of Bi, O, and C (Fig. S1). As displayed in Fig. 1c, a spin-orbit split doublet with binding energies of Bi $4f_{7/2}$ at 159.0 eV and Bi $4f_{5/2}$ at 164.3 eV can be seen, corresponding to Bi^{3+} cations coordinated by nine oxygen atoms (eight oxygen atoms from the carboxylate species of the BTC^{3-} and one coordinating oxygen atom from the terminal water molecule) in the MOF [33]. The O 1s peaks at 531.1 and 533.5 eV are attributed to Bi-O bond and the O in bismuth-oxo clusters of Bi-MOF, respectively (Fig. 1d). Shown in Fig. 1e are N_2 adsorption-desorption isotherms of the Bi-MOF. A typical type I -isotherm is observed according to the BDDT (Brunauer, Deming, Deming, and Teller) classification [34], where the sharp adsorption in the relative pressure (P/P_0) range $\leq$ 0.01 originates from significant microporosity of the MOF structure. The average pore diameter based on the desorption branch of the isotherm was determined to be about 0.8 nm (inset of Fig. 1e), close to the accessible size of the hexagonal channels in the Bi-MOF. The BET (Brunauer-Emmett-Teller) surface area and single-point total pore volume of the Bi-MOF are 316.8 $m^2 g^{-1}$ and 0.144 $cm^3 g^{-1}$, respectively. Notably, the as-made Bi-MOF possesses a CO_2 adsorption capacity of 33.0 $mg_{CO2}\ g_{cat.}^{-1}$ at 298 K and 1 atm, two times higher than that of the Bi sheets (Fig. 1f). Such remarkable adsorption of CO_2 in Bi-MOF likely arises from the large number of hexagonal, rectangular, and triangular channels in its crystal structure with accessible diameters bigger than the molecule size of CO_2. The superior CO_2 uptake capability evidently facilitates the adsorption of a large amount of CO_2 on the Bi-MOF catalyst surface, thus potentially promoting higher catalytic turnover.

Further morphological characterization by SEM, TEM together with energy-dispersive X-ray spectroscopy (EDS), and HAADF-STEM revealed that the Bi-MOF sample is made up of thin flakes that randomly stack on top of each other (Fig. 2 and Fig. S2). Shown in Fig. 2d is a transformed TEM image with different colors to manifest thickness distributions of the sheets. EDS elemental maps (Fig. 2b,f–h and Fig. S2d-f) along with EDS spectrum (Fig. S2g) confirm the uniform distribution of Bi, C, and O elements throughout the sheets. High-resolution TEM observation (Fig. 2i) and fast Fourier transformation (FFT) (inset of Fig. 2c) indicate good crystallinity of the MOF nanosheets. But the crystals are electron beam sensitive and would thus deform during TEM measurements.

3.2. Electrocatalytic properties

ECR is sensitive to operating conditions, such as the nature and properties of the electrocatalyst, electrolyte composition, and electrochemical cell type [26,35]. To assess the intrinsic catalytic properties of the as-prepared Bi-MOF, we conducted electrochemical CO_2 reduction tests in CO_2-saturated 0.1 M $KHCO_3$ aqueous electrolyte (pH 6.8) using a reported design of liquid H-type cell separated by a cation-exchange membrane (Nafion 117) with continuous CO_2 bubbling [36]. The gas-phase products were identified and quantified by gas chromatography. Liquid products in the solution formed during CO_2 reduction were determined by proton nuclear magnetic resonance. All potentials here are referenced to the RHE scale unless specified otherwise. Shown in Fig. 3a are polarization curves of Bi-MOF in 0.1 M $KHCO_3$ saturated with Ar or CO_2. A reductive current is observed to increase sharply at potentials below ~ –0.6 V, suggesting the predominant occurrence of CO_2 reduction. The Bi-MOF exhibits over two times higher current density in the CO_2-saturated solution than that of HER from ~ –0.6 to ~ –1.2 V recorded during Ar purging. In the potential range of ~ –0.6 to ~ –1.1 V, both Bi-MOF and bulk Bi_2O_3 were found to suppress CO formation and the detected products are only HCOOH and H_2, though trace amounts of CO were also identified for Bi sheets in CO_2-saturated 0.1 M $KHCO_3$. For experiments conducted in Ar-saturated 0.1 M $KHCO_3$ (CO_2-free electrolyte), no HCOOH was detectable, confirming the selective electrosynthesis of HCOOH solely through the ECR. The Faradaic efficiencies for H_2 and CO formation attained with the three catalysts are provided in Fig. S3. As illustrated in Fig. 3b, the conversion

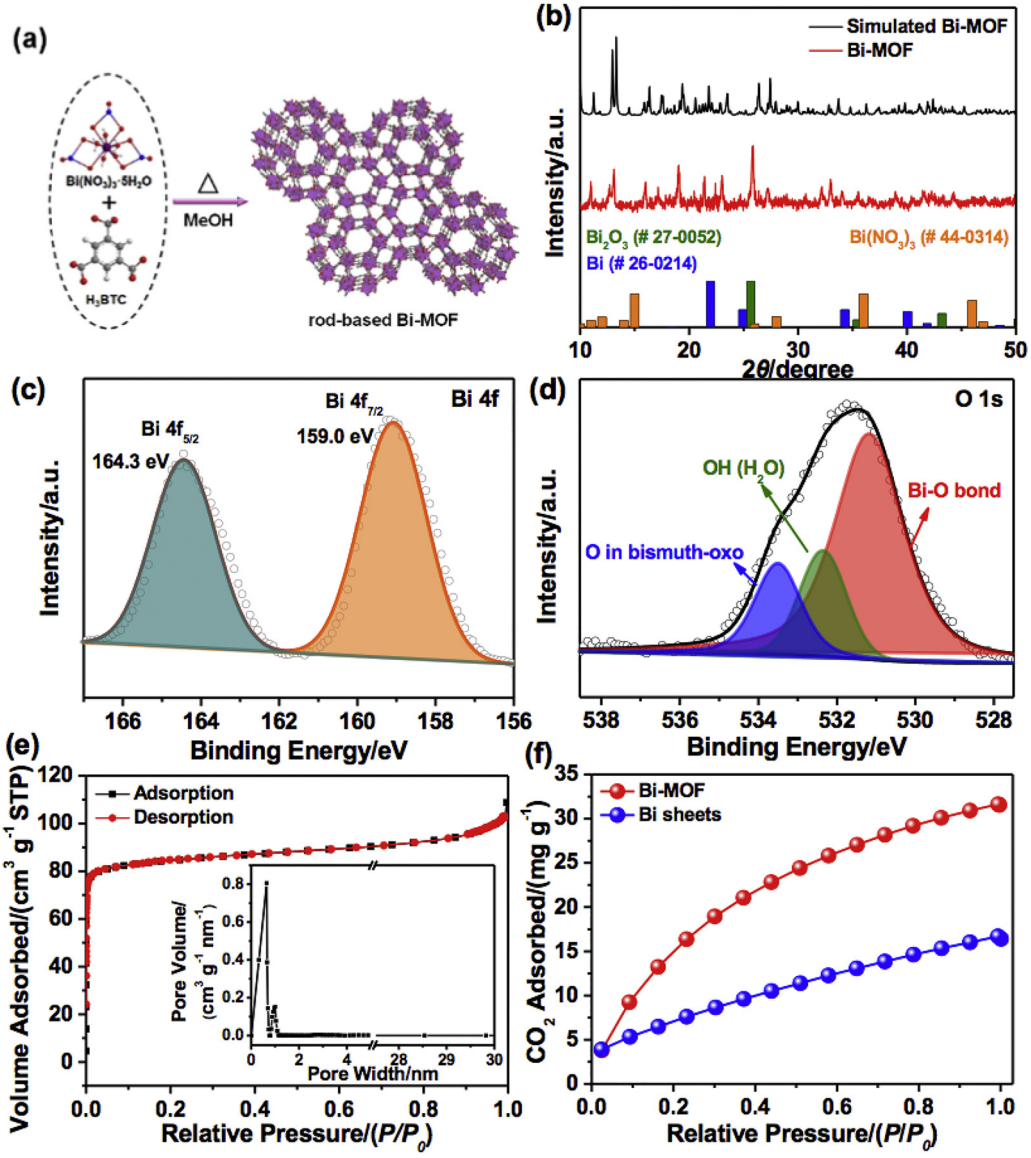

Fig. 1. (a) Schematic depiction of the formation of Bi-MOF. Bismuth – oxygen polyhedra shown in the MOF crystal structure are indicated in purple. (b) XRD patterns of Bi-MOF and simulated Bi-MOF. Discrepancies in intensities and some positions may be attributed to the disordered guest species in the pores that have not been considered in the crystal structure model. (c) Bi 4f and (d) O 1s XPS spectra of Bi-MOF. (e) N_2 adsorption/desorption isotherms of Bi-MOF. (f) CO_2 adsorption isotherms of Bi-MOF and Bi sheets (For interpretation of the references to colour in this figure legend, the reader is referred to the web version of this article.).

of CO_2 to HCOOH over the Bi-MOF electrode begins at a potential of about ~ –0.6 V (with an HCOOH partial current density > 0.3 mA cm^{-2}) and increases to a maximum (92.2 %) at ~ –0.9 V, comparable to recently reported ultrathin Bi nanosheets [22], Bi nanoparticles on Sb nanosheets [24], and Bi_2O_3 crystals [25] under similar overpotentials in an H-type cell. At wide applied cathodic potentials ranging from ~ –0.8 to ~ –1.1 V, HCOOH is generated in substantial quantities with *FE* surpassing 85.0 %. In contrast, a significant drop in HCOOH yield occurs with increasing overpotential > 0.65 V for both Bi sheets and bulk Bi_2O_3 (Their XRD patterns, SEM, and TEM images are displayed in Fig. S4), affording *FE*s being less than 38.7 % at ~ –1.1 V. Alternatively, HCOOH partial current density increased with the overpotential reaching as high as 15.0 mA cm^{-2} (41.0 mA mg^{-1} when normalized with Bi loading according to the formula of Bi-MOF, $Bi_9(C_9H_3O_6)_9(H_2O)_9$ [33]) at ~ –1.1 V. Given the corresponding energy-storing reaction and equilibrium potential (–0.225 V *vs.* RHE) [37], Bi-MOF delivers a remarkable cathodic energetic efficiency (*EE*) of about 63.0 %. It is worthy to note that the onset potential, *FE*, partial current density, and *EE* of HCOOH across potentials tested in this study on Bi-MOF substantially outperformed those of the commercial Bi sheets, Bi_2O_3, and pure carbon fiber support (Fig. 3b-d).

To further elucidate the superior activity of Bi-MOF, the electrochemical active surface area (ECSA), Tafel slope, and electrochemical impedance were studied [38]. The double-layer capacitance as an approximation of the ECSA indicated that Bi-MOF has significantly higher ECSA than that of both Bi sheets and Bi_2O_3 (Fig. S5), which is beneficial for HCOOH formation. Likewise, Bi-MOF exhibited a dramatically higher HCOOH formation with TOF of 526.9 h^{-1} at ~ –0.9 V, as compared to 86.5 and 28.4 h^{-1} for bulk Bi_2O_3 and Bi sheets, respectively (Fig. 3e). The Tafel plots of CO_2 reduction on the various catalysts, representing the kinetics of HCOOH formation and possible reaction mechanism are provided in Fig. 3f. The Tafel slope was 175.5 mV dec^{-1} for Bi-MOF, lower than 186.3 mV dec^{-1} for Bi sheets and 250.4 mV dec^{-1} for bulk Bi_2O_3, indicating faster kinetics of the ECR on Bi-MOF compared to the other two catalysts. This also implies that the first electron transfer for the formation of *HCOO intermediate on the surface of the catalysts is the rate-determining step. The Nyquist plots in Fig. 3g manifest that Bi-MOF has lower charge transfer resistance (R_{ct})

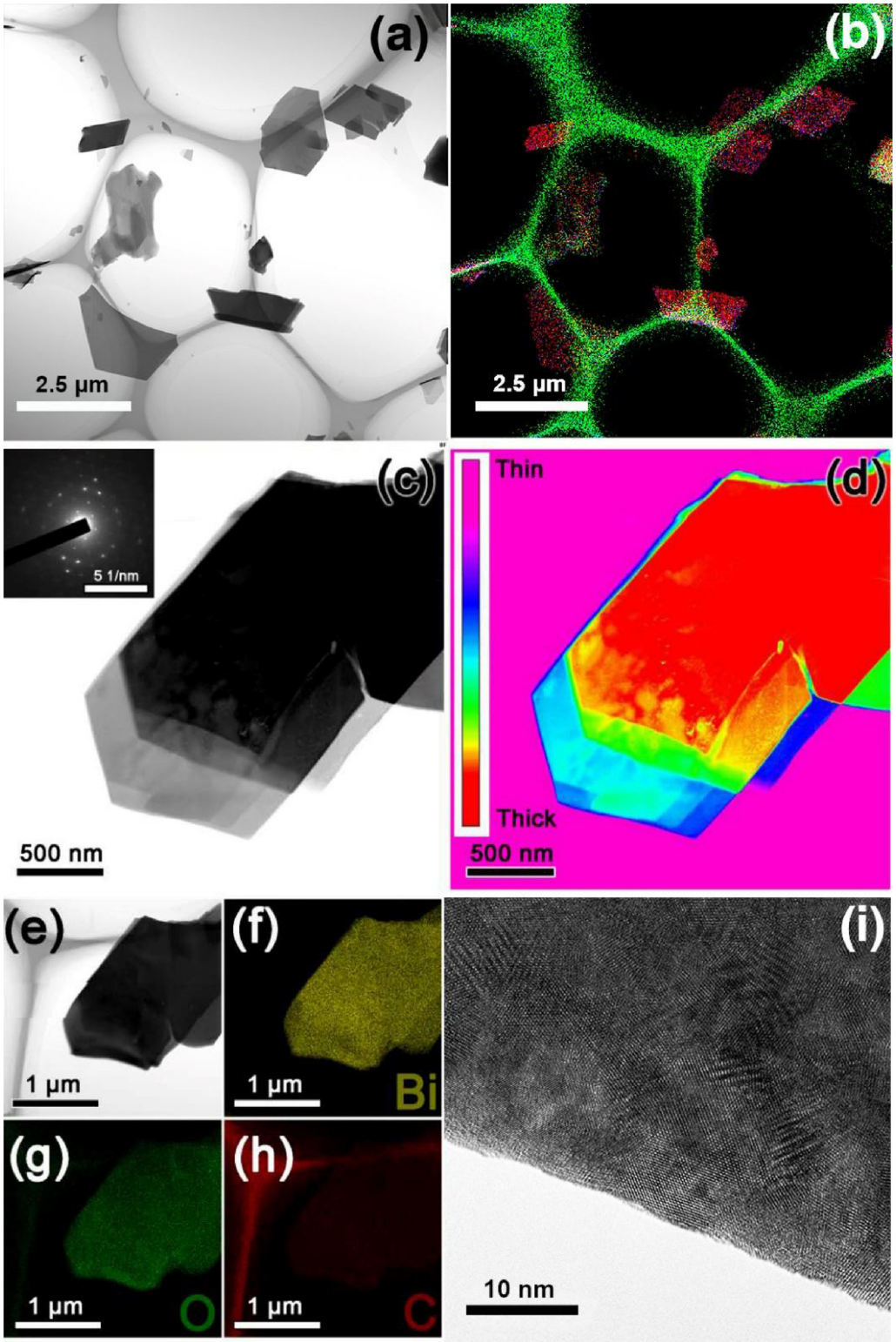

Fig. 2. (a) Low-magnification TEM image Bi-MOF sheets. (b) EDS elemental map of overlay of Bi (red), C (green) and O (blue) over the region shown in image (a). (c) High-magnification TEM image of stacked Bi-MOF sheets. Inset: FFT of the image. (d) Transformed TEM image of part c, showing thickness distributions of the sheets. (e) TEM image of Bi-MOF sheets and corresponding EDS maps of (f) Bi, (g) O, and (h) C. (i) HRTEM image of a Bi-MOF nanosheet (For interpretation of the references to colour in this figure legend, the reader is referred to the web version of this article.).

compared with the other two samples, favoring charge exchange between the catalyst and reactants in the electrolyte.

The long-term performance of Bi-MOF was investigated at a constant potential of –0.9 V for 10 h. The yield of HCOOH was found to increase monotonically with reaction time, indicating excellent stability of the catalyst (Fig. 3h). Alternated electrolysis cycling measurements between Ar- and CO_2-saturated electrolytes show that the evolved HCOOH arises from the feed gas CO_2 and is stable over 8 cycles (Fig. 3i). In addition, the Bi-MOF catalyst preserves its selectivity for HCOOH production and shows stable reduction current even after 30 h

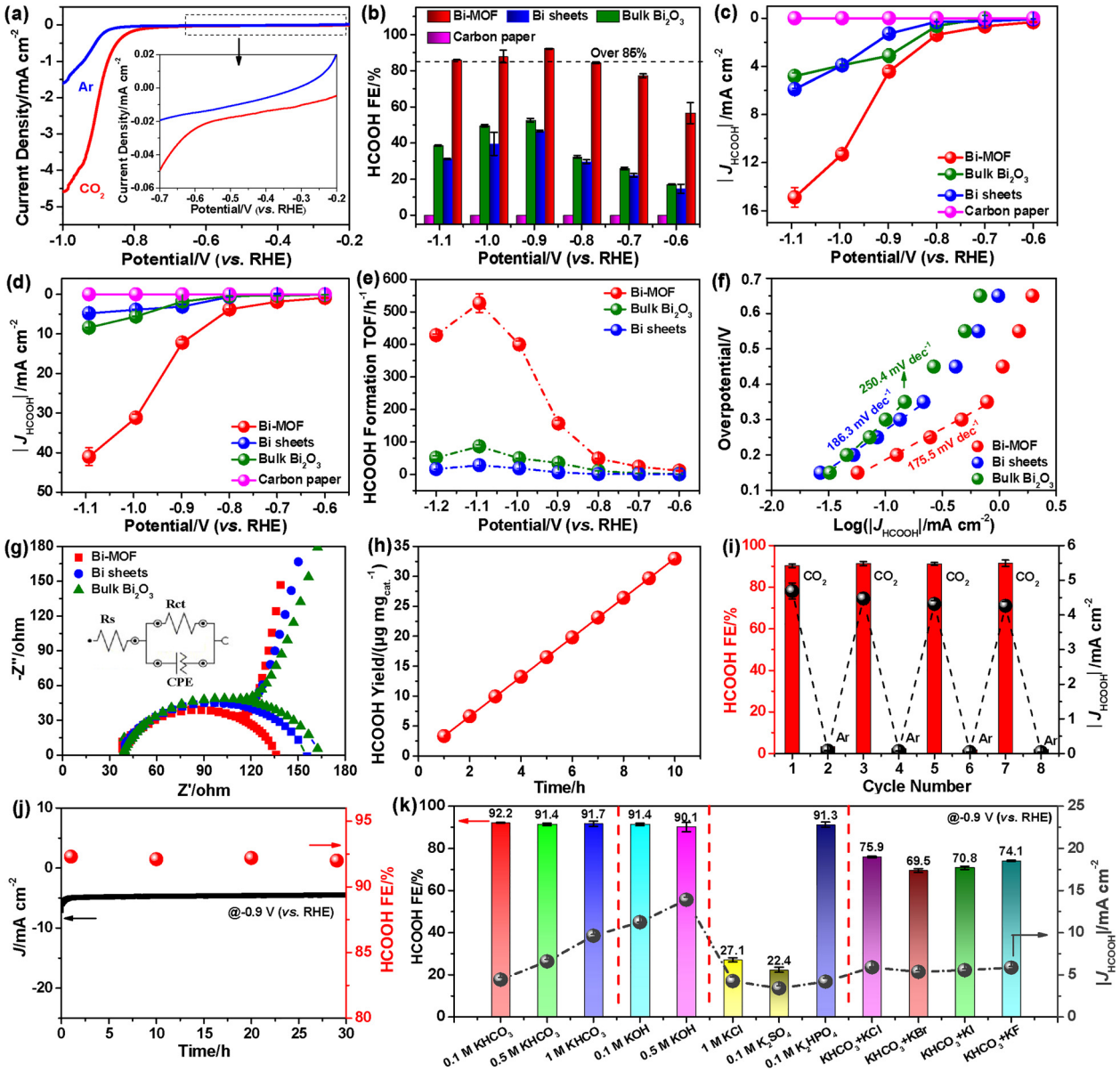

Fig. 3. (a) Linear sweep voltammetry (LSV) results of Bi-MOF in Ar- (blue line) or CO_2- (red line) saturated 0.1 M $KHCO_3$ solution with a scan rate of 5 mV s^{-1}. The inset highlights the LSV curves in the potential range from ~ –0.2 to ~ –0.7 V. (b) HCOOH *FEs*, (c) HCOOH partial current densities, and (d) mass activities of Bi-MOF, Bi sheets, bulk Bi_2O_3, and carbon paper electrodes within a potential window of ~ –0.6 to ~ –1.1 V in CO_2-saturated 0.1 M $KHCO_3$ solution. (e) TOFs and (f) Tafel plots for HCOOH production, and (g) EIS spectra of Bi-MOF, Bi sheets, and bulk Bi_2O_3. (h) HCOOH yield against electrolysis time over Bi-MOF at ~ –0.9 V. (i) HCOOH *FEs* and corresponding partial current densities for Bi-MOF during cycles with an interval of 1 h in CO_2- and Ar-saturated 0.1 M $KHCO_3$ at ~ –0.9 V. (j) Current density and HCOOH *FE* of Bi-MOF during long-time electrolysis at ~ –0.9 V. (k) HCOOH *FEs* (column) and HCOOH partial current densities (grey ball) of Bi-MOF in various electrolytes with different concentrations (For interpretation of the references to colour in this figure legend, the reader is referred to the web version of this article.).

of continuous potentiostatic electrolysis (Fig. 3j and Fig. S6). N_2 adsorption-desorption measurements indicate that the microporosity of the Bi-MOF catalyst was largely retained regardless of electrolysis (Fig. S7).

By modulating the solvothermal temperature, it was possible to regulate the ECR activity of the catalysts. The Bi-MOF catalyst synthesized at 120 °C was found to exhibit the best activity for ECR (Fig. S8). To probe the nature of the active sites in the Bi-MOF catalysts, a series of control experiments were performed (Fig. S9). The catalyst formed in the absence of a bismuth precursor showed very low ECR activity for HCOOH generation. This confirms the critical role of bismuth toward CO_2 reduction to produce HCOOH. Similarly, the Bi_2O_3 sample obtained without the H_3BTC ligand displayed partial ECR activity, but it was not as active as the Bi-MOF catalyst. This highlights the important role of the MOF structure during CO_2 reduction, which can also be corroborated by the decay of ECR performance over the Bi-MOF annealed in argon at 700 °C for 2 h. When the H_3BTC ligand was replaced with terephthalic acid (TPA), 2-aminoterephthalic acid (ATPA), 2,5-dichloroterephthalic acid (DCTPA), 1,3,5-tri (4-carboxyphenyl) benzene, or biphenyl-3,3',5,5'-tetracarboxylic acid, the ECR activity of Bi-MOFs all dropped, probably due to the reduction of the number of Bi^{3+} cations and coordinated anions in the asymmetric unit. Therefore, the highly efficient performance could result from a combined impact: 1) The highly exposed 2D structure with hierarchical porosity facilitated rapid mass transport; 2) Abundant intrinsic micropores confined CO_2 molecules, ensuring sufficient local CO_2

concentration for subsequent reduction; 3) The uniformly distributed and accessible Bi(3+) may have provided the major active sites toward CO_2 activation and transformation.

The effect of the nature of the electrolyte on the ECR performance of the catalyst was examined in $KHCO_3$ and KOH with different concentrations, as well as in the mixed electrolytes. Note that the HCOOH partial current density increases with the increase of the electrolyte concentration, approaching 14.0 mA cm^{-2} at ~ –0.9 V in 1.0 M KOH (Fig. 3k), while the HCOOH *FE* remained essentially unchanged. Further, we found that the addition of halide (F^-, Cl^-, Br^-, and I^-) and SO_4^{2-} ions in catholyte led to a drastic decrease of HCOOH *FE*. This may be associated with the strong adsorption of halides and SO_4^{2-} on the surface of the Bi-MOF electrode, thus inhibiting the adsorption of K^+ and CO_2 on the cathode surface. Meanwhile, the potential difference of the dispersed layer in the electric double layer will increase owing to the increased amounts of the negative charge on the electrode surface. This favors the transport of polar water molecules instead of nonpolar CO_2 molecules to the cathode surface, thereby promoting the competitive HER and hindering ECR.

3.3. Operando and ex-situ X-ray absorption fine structure analysis

X-ray absorption fine structure (XAFS) spectra of Bi-MOF at Bi L_3-edge prior to electrocatalysis, during *in-situ* electrochemical CO_2 reduction and consequently after 10 h electrolysis are compared in Fig. 4. Specifically, operando measurements (Fig. 4a-b) are provided to observe changes in electronic structure as a function of electrochemical bias and CO_2 electroreduction time, while Fig. 4c-d portrays XAFS of Bi-MOF after long-term electrochemical CO_2 reduction to investigate any structural changes associated with post-electrocatalysis. Please refer to the experimental conditions in the Supporting Information for further details. Fig. 4a shows operando normalized X-ray absorption near-edge structure (XANES) of Bi-MOF during CO_2 electroreduction at OCV, at ~ –0.9 V, and another after 90 min of continuous bias at –0.9 V.

XANES spectra of electrochemically biased Bi-MOF, both at OCV and at ~ –0.9 V juxtaposed with the XANES spectrum of Bi_2O_3 as reference confirms the overall oxidation state of Bi-MOF to be close to three (Bi^{3+}). However, upon CO_2 electroreduction at ~ –0.9 V for 90 min, a slight but discernible negative shift in the Bi-MOF XANES spectra was observed (inset in the edge-transition region of Fig. 4a). The results indicate that the oxidation state of Bi (Bi^{3+}) remained apparently unchanged under the applied electrochemical CO_2 reduction conditions. However, a further negative shift in the *ex-situ* XANES electrode was evident after a prolonged CO_2 reduction for 10 h, as shown in Fig. 4c. This shift is significant (2 − 3 eV negative compared to Bi_2O_3 reference) and indicates the partial reduction of Bi in the Bi-MOF catalyst. On the contrary, CO_2 reduction based electrocatalysts of 2D Bi nanosheet [39], Bi_2O_3 nanotube [40], Bi_2S_3 rod-like branch [41], and 2D BiOBr [42] structures reported elsewhere were rather quickly and completely reduced from Bi(+3) to metallic Bi(0) upon only 1 h of a rather low electrochemical bias < –0.24 V (*vs.* RHE). Therefore, the MOF structure plays a critical role in maintaining Bi in the (+3) oxidation state during long-term electrochemical CO_2 reduction. Moreover, higher selectivity and TOF along with lower Tafel slope observed for Bi-MOF when compared to Bi sheets and bulk Bi_2O_3 also attest to the unique ability of Bi-MOF to maintain its structure and oxidation-state for long-term electrolysis.

On the other hand, Fourier transform (FT) of EXAFS oscillations of all Bi-MOF based *in-situ* electrochemical measurements are presented in Fig. 4b. A high-intense signature peak near 1.6 Å corresponding Bi-O coordination-sphere along with oscillations around 3.6 Å associated with Bi-Bi coordination which experimentally corroborates the presence of the Bi^{3+} oxidation-state in Bi-MOF. The relative peak intensity of Bi-O oscillations slowly declined when the electrochemical potential changed from OCV to ~ –0.9 V and also after constant CO_2 reduction for 90 min (at ~ –0.9 V). Furthermore, FT oscillations of *ex-situ* electrodes of Fig. 4d depicts a much higher reduction in Bi-O oscillations (*ca.* 1.6 Å) along with the development of well-defined Bi-Bi oscillations of metallic-Bi between 2.5–3.5 Å. This experimental evidence re-affirms the partial conversion of Bi-MOF from Bi^{3+} to Bi° upon long-term CO_2 reduction for 10 h. Provided in Table S1 is a summary of parameters of the sample including interatomic distances (*R*) and coordination numbers (*N*) obtained during EXAFS curve modeling based on *ex-situ* analysis of Bi-MOF electrodes. Consequently, the Bi-Bi coordination number of long-term electrolyzed Bi-MOF (3.7 ± 1.3) has significantly reduced compared with the pristine Bi-MOF electrode (6.2 ± 2.1). These experimental findings also well agree and complement XPS analysis provided in the previous section (Fig. 1d).

3.4. Density functional theory calculations

In our DFT calculations, we considered thermochemistry of the CO, HCOOH, and H_2 formation pathway, as shown in Fig. 5. We find that three binding sites behave similarly in terms of energetics (Fig. 5b). Notably, *COOH is an intermediate to form CO, but *COOH does not bind at the binding site (Fig. 5c). This indicates that *COOH is not formed from CO_2 and H^+, explaining the low selectivity towards deoxygenated species (e.g., CO, CH_4, CH_3OH). On the other hand, *HCOO, an intermediate for the formation HCOOH, reactively binds with 1.88 eV, which is in-line with the experimental overpotential needed to observe the activity. Our calculations suggest that HER is suppressed over Bi-MOF, as the *H formation energy is 2.27 eV, 0.39 eV larger than *HCOO formation. Overall, these calculation results provide a rationale for the activity, selectivity, and overpotential trends of the Bi-MOF catalyst.

4. Conclusions

In summary, we have demonstrated a 2D porous Bi-MOF catalyst for highly active, selective, and stable electrochemical CO_2 reduction under ambient conditions. A remarkable Faradaic efficiency of 92.2 % for HCOOH formation was achieved at an overpotential of 0.65 V with an exceptional stability over 30 h. Operando and *ex-situ* synchrotron-radiation characterization and theoretical calculations suggested that the highly accessible Bi(3+) and the unique one-dimensional channels in the Bi-MOF played vital roles in the enhancement of CO_2 adsorption and HCOOH conversion. This work highlights new possibilities for developing unique novel framework structures for efficient electrochemical CO_2 reduction.

CRediT authorship contribution statement

Fang Li: Data curation, Formal analysis. **Geun Ho Gu:** Data curation, Formal analysis. **Changhyeok Choi:** Data curation, Formal analysis. **Praveen Kolla:** Data curation, Formal analysis, Investigation, Writing - review & editing. **Song Hong:** Data curation, Formal analysis. **Tai-Sing Wu:** Data curation, Formal analysis. **Yun-Liang Soo:** Data curation, Formal analysis. **Justus Masa:** Writing - review & editing. **Sanjeev Mukerjee:** Data curation, Formal analysis. **Yousung Jung:** Funding acquisition, Investigation, Writing - review & editing. **Jieshan Qiu:** . **Zhenyu Sun:** Conceptualization, Funding acquisition, Investigation, Supervision, Writing - review & editing.

Declaration of Competing Interest

The authors declare that they have no known competing financial interests or personal relationships that could have appeared to influence the work reported in this paper.

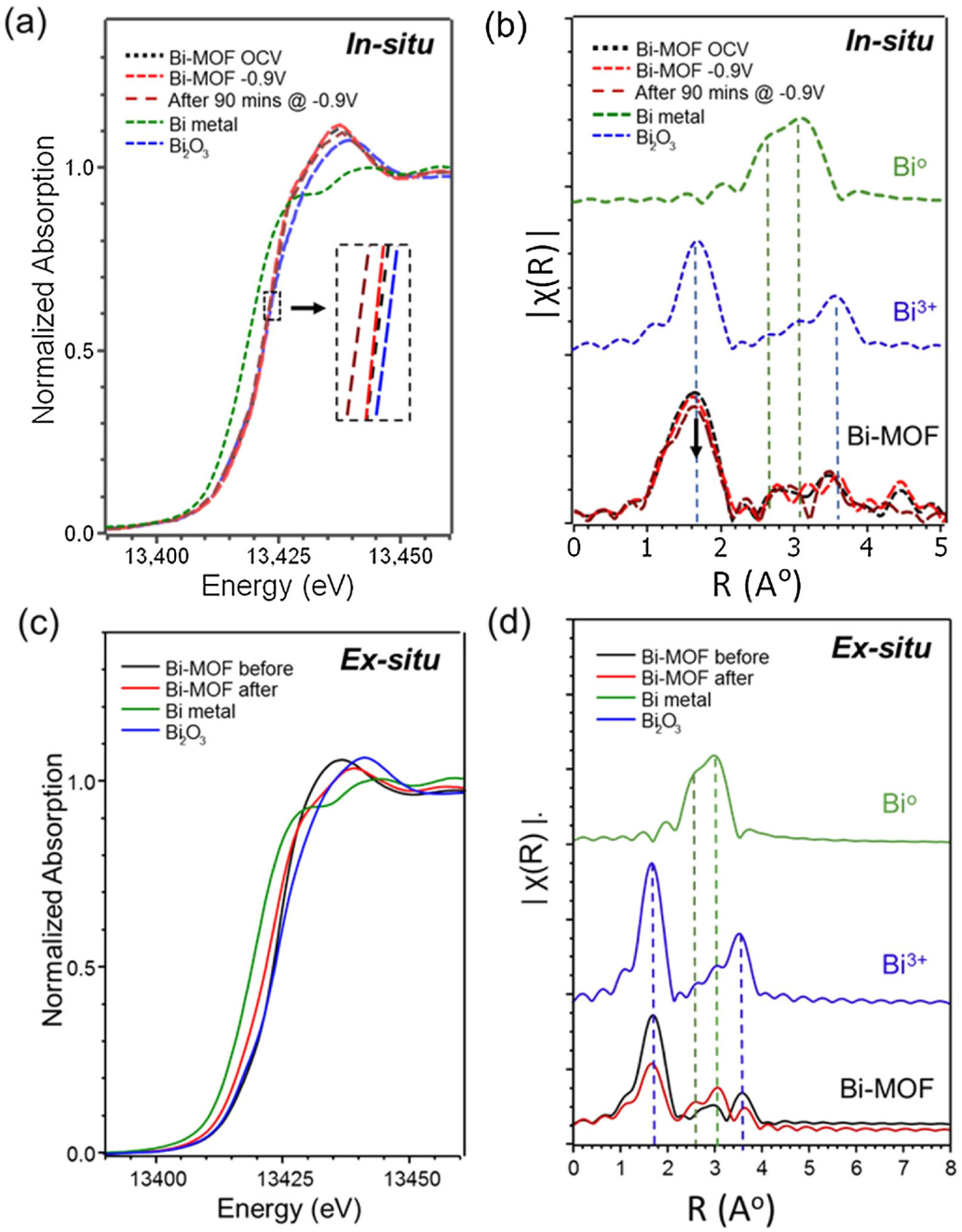

Fig. 4. Comparison of Bi L_3-edge X-ray absorption fine structure (XAFS) of Bi-MOF along with those for Bi metal and Bi_2O_3 as reference standards: (a) and (b) represent their respective XANES and Fourier transform of EXAFS spectrum as a function of electrochemical bias and with electroreduction time under *in-situ* electrochemical CO_2 reduction conditions. Whereas (c) and (d) reveal their corresponding *ex-situ* XAFS of Bi-MOF electrodes before and after CO_2 electrocatalysis for 10 h.

Acknowledgements

This work was supported by the National Natural Science Foundation of China (No. 21972010); Beijing Natural Science Foundation (No. 2192039); the State Key Laboratory of Organic–Inorganic Composites (No. oic-201901001); and Beijing University of Chemical Technology (XK180301). Y.J. acknowledges the support from National Research Foundation of Korea (NRF-2019M3D3A1A01069099). XAS analysis presented in this manuscript used resources of 6BM-BMM and 7BM-QAS of the National Synchrotron Light Source II, a U.S. Department of Energy (DOE) Office of Science User Facility operated for the DOE Office of Science by Brookhaven National Laboratory under Contract No. DE-SC0012704. We greatly acknowledge the experimental support from lead beamline scientist Dr. Steven Ehrlich (7BM) and Dr. Bruce Ravel (6BM) during XAS analysis. F.L. designed the experiments. S.H. carried out TEM characterization. P.K., T.W., Y.S., and S.M. conducted XAFS measurements and analysis. G.G., C.C., and Y.J. performed DFT calculations. J.M. assisted with language correction. Z.S. supervised the entire project and wrote the manuscript. All authors discussed the results.

Appendix A. Supplementary data

Supplementary material related to this article can be found, in the online version, at doi:https://doi.org/10.1016/j.apcatb.2020.119241.

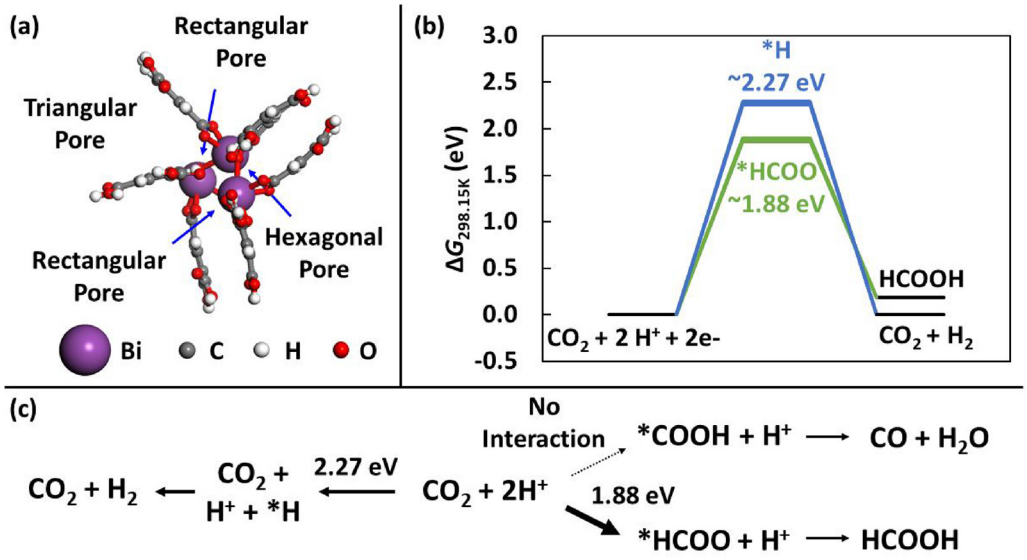

Fig. 5. (a) Simulated cluster representing Bi-MOF catalytic sites. Blue arrows show the binding sites of adsorbates. (b) Free energy diagram of hydrogen evolution reaction and formic acid formation. The ~ energy value indicates the average energy of the three binding sites. (c) Suggested reaction pathway. Each arrow indicates a reaction with an addition of an electron. *COOH, an intermediate for CO formation, does not bind (For interpretation of the references to colour in this figure legend, the reader is referred to the web version of this article.).

References

[1] P. De Luna, C. Hahn, D. Higgins, S.A. Jaffer, T.F. Jaramillo, E.H. Sargent, What would it take for renewably powered electrosynthesis to displace petrochemical processes? Science 364 (2019) eaav3506.

[2] M. Jia, Q. Fan, S. Liu, J. Qiu, Z. Sun, Single-atom catalysis for electrochemical CO_2 reduction, Curr. Opin. Green Sustain. Chem. 16 (2018) 1–6.

[3] J. Gu, C. Hsu, L. Bai, H. Chen, X. Hu, Atomically dispersed Fe^{3+} sites catalyze efficient CO_2 electroreduction to CO, Science 364 (2019) 1091–1094.

[4] Q. Fan, M. Zhang, M. Jia, S. Liu, J. Qiu, Z. Sun, Electrochemical CO_2 reduction to C_{2+} species: heterogeneous electrocatalysts, reaction pathways, and optimization strategies, Mater. Today Energy 10 (2018) 280–301.

[5] M. Jia, C. Choi, T. Wu, C. Ma, P. Kang, H. Tao, Q. Fan, S. Hong, S. Liu, Y. Soo, Y. Jung, J. Qiu, Z. Sun, Carbon-supported Ni nanoparticles for efficient CO_2 electroreduction, Chem. Sci. 9 (2018) 8775–8780.

[6] H. Tao, X. Sun, S. Back, Z. Han, Q. Zhu, T. A.W.Robertson, Q. Ma, B. Fan, Y. Han, Z. Jung, Sun, Doping palladium with tellurium for the highly selective electrocatalytic reduction of aqueous CO_2 to CO, Chem. Sci. 9 (2018) 483–487.

[7] Q. Fan, P. Hou, C. Choi, T. Wu, S. Hong, F. Li, Y. Soo, P. Kang, Y. Jung, Z. Sun, Activation of Ni particles into single Ni-N atoms for efficient electrochemical reduction of CO_2, Adv. Energy Mater. 123 (2019) 1903068.

[8] M. Jia, S. Hong, T. Wu, X. Li, Y. Soo, Z. Sun, Single Sb sites for efficient electrochemical CO_2 reduction, Chem. Commun. 55 (2019) 12024–12027.

[9] Z. Sun, N. Talreja, H. Tao, J. Texter, M. Muhler, J. Strunk, J. Chen, Catalysis of carbon dioxide photoreduction on nanosheets: fundamentals and challenges, Angew. Chem. Int. Ed. 57 (2018) 7610–7627.

[10] Z. Sun, T. Ma, H. Tao, Q. Fan, B. Han, Fundamentals and challenges of electrochemical CO_2 reduction using two-dimensional materials, Chem 3 (2017) 560–587.

[11] Y. Gao, S. Liu, Z. Zhao, H. Tao, Z. Sun, Heterogeneous catalysis of CO_2 hydrogenation to C_{2+} products, Acta Phys. -Chim. Sin. 34 (2018) 858–872.

[12] T. Ma, Q. Fan, X. Li, J. Qiu, T. Wu, Z. Sun, Graphene-based materials for electrochemical CO_2 reduction, J. CO_2 Util. 30 (2019) 168–182.

[13] T. Ma, Q. Fan, H. Tao, Z. Han, M. Jia, Y. Gao, W. Ma, Z. Sun, Heterogeneous electrochemical CO_2 reduction using nonmetallic carbon-based catalysts: current status and future challenges, Nanotechnology 28 (2017) 472001.

[14] S. Gao, Y. Lin, X. Jiao, Y. Sun, Q. Luo, W. Zhang, D. Li, J. Yang, Y. Xie, Partially oxidized atomic cobalt layers for carbon dioxide electroreduction to liquid fuel, Nature 529 (2016) 68–71.

[15] F. Li, M. Xue, J. Li, X. Ma, L. Chen, X. Zhang, D.R. MacFarlane, J. Zhang, Unlocking the electrocatalytic activity of antimony for CO_2 reduction by two-dimensional engineering of the bulk material, Angew. Chem. Int. Ed. 56 (2017) 14718–14722.

[16] X. Zu, X. Li, W. Liu, Y. Sun, J. Xu, T. Yao, W. Yan, S. Gao, C. Wang, S. Wei, Efficient and robust carbon dioxide electroreduction enabled by atomically dispersed $Sn\delta^+$ sites, Adv. Mater. 31 (2019) 1808135.

[17] W. Deng, L. Zhang, L. Li, S. Chen, C. Hu, Z. Zhao, T. Wang, J. Gong, Crucial role of surface hydroxyls on the activity and stability in electrochemical CO_2 reduction, J. Am. Chem. Soc. 141 (2019) 2911–2915.

[18] B. Jiang, X. Zhang, K. Jiang, D. Wu, W. Cai, Boosting formate production in electrocatalytic CO_2 reduction over wide potential window on Pd surfaces, J. Am. Chem. Soc. 140 (2018) 2880–2889.

[19] F. Pan, H. Zhang, K. Liu, D. Cullen, K. More, M. Wang, Z. Feng, G. Wang, G. Wu, Y. Li, Unveiling active sites of CO_2 reduction on nitrogen-coordinated and atomically dispersed iron and cobalt catalysts, ACS Catal. 8 (2018) 3116–3122.

[20] D. Gao, H. Zhou, F. Cai, J. Wang, G. Wang, X. Bao, Pd-containing nanostructures for electrochemical CO_2 reduction reaction, ACS Catal. 8 (2018) 1510–1519.

[21] T. Zhang, X. Li, Y. Qiu, P. Su, W. Xu, H. Zhong, H. Zhang, Multilayered Zn nanosheets as an electrocatalyst for efficient electrochemical reduction of CO_2, J. Catal. 357 (2018) 154–162.

[22] N. Han, Y. Wang, H. Yang, J. Deng, J. Wu, Y. Li, Y. Li, Ultrathin bismuth nanosheets from in situ topotactic transformation for selective electrocatalytic CO_2 reduction to formate, Nat. Commun. 9 (2018) 1320.

[23] E. Zhang, T. Wang, K. Yu, J. Liu, W. Chen, A. Li, H. Rong, R. Lin, S. Ji, X. Zheng, Y. Wang, L. Zheng, C. Chen, D. Wang, J. Zhang, Y. Li, Bismuth single atoms resulting from transformation of metal–organic frameworks and their use as electrocatalysts for CO_2 reduction, J. Am. Chem. Soc. 141 (2019) 16569.

[24] G. Wen, D.U. Lee, B. Re, F.M. Hassan, G. Jiang, Z.P. Cano, J. Gostick, E. Croiset, Z. Bai, L. Yang, Z. Chen, Carbon dioxide electroreduction: orbital interactions in Bi-Sn bimetallic electrocatalysts for highly selective electrochemical CO_2 reduction toward formate production, Adv. Energy Mater. 8 (2018) 1802427.

[25] P. Deng, H. Wang, R. Qi, J. Zhu, S. Chen, F. Yang, L. Zhou, K. Qi, H. Liu, B.Y. Xia, Bismuth oxides with enhanced bismuth–oxygen structure for efficient electrochemical reduction of carbon dioxide to formate, ACS Catal. 10 (2020) 743–750.

[26] P. Deng, F. Yang, Z. Wang, S. Chen, Y. Zhou, S. Zaman, B.Y. Xia, Metal–organic framework-derived carbon nanorods encapsulating bismuth oxides for rapid and selective CO_2 electroreduction to formate, Angew. Chem. 132 (2020), https://doi.org/10.1002/anie.202000657.

[27] J. Zhou, K. Yuan, L. Zhou, Y. Guo, M. Luo, X. Guo, Q. Meng, Y. Zhang, Boosting electrochemical reduction of CO_2 at a low overpotential by amorphous Ag-Bi-S-O decorated Bi° nanocrystals, Angew. Chem. Int. Ed. 131 (2019) 14197–14201.

[28] Z. Yin, D. Ga, S. Yao, B. Zhao, F. Cai, L. Lin, P. Tang, P. Zhai, G. Wang, D. Ma, Highly selective palladium-copper bimetallic electrocatalysts for the electrochemical reduction of CO_2 to CO, Nano Energy 27 (2016) 35–43.

[29] C. Zhao, X. Dai, T. Yao, W. Chen, X. Wang, J. Wang, J. Yang, S. Wei, Y. Wu, Y. Li, Ionic exchange of metal-organic frameworks to access single nickel sites for efficient electroreduction of CO_2, J. Am. Chem. Soc. 139 (2017) 8078–8081.

[30] W. Ju, A. Bagger, G. Hao, A.S. Varela, I. Sinev, V.B.R. Cuenya, S. Kaskel, J. Rossmeisl, P. Strasser, Understanding activity and selectivity of metal-nitrogen-doped carbon catalysts for electrochemical reduction of CO_2, Nat. Commun. 8 (2017) 944.

[31] F. Pan, W. Deng, C. Justiniano, Y. Li, Identification of champion transition metals centers in metal and nitrogen-codoped carbon catalysts for CO_2 reduction, Appl. Catal. B Environ. 226 (2018) 463–472.

[32] A.K. Inge, M. Koppen, J. Su, M. Feyand, H. Xu, X. Zou, M. O'Keeffe, N. Stock, Unprecedented topological complexity in a metal-organic framework constructed from simple building units, J. Am. Chem. Soc. 138 (2016) 1970–1976.

[33] H. Ouyang, N. Chen, G. Chang, X. Zhao, Y. Sun, S. Chen, H. Zhang, D. Yang, Selective capture of toxic selenite anions by bismuth-based metal-organic frameworks, Angew. Chem. Int. Ed. 57 (2018) 13197–13201.

[34] S.J. Gregg, K.S.W. Sing, Academic Press 86 (1982) 957.

[35] C. Zhao, Y. Wang, Z. Li, W. Chen, Q. Xu, D. He, D. Xi, Q. Zhang, T. Yuan, Y. Qu, J. Yang, F. Zhou, Z. Yang, X. Wang, J. Wang, J. Luo, Y. Li, H. Duan, Y. Wu, Y. Li, Solid-diffusion synthesis of single-atom catalysts directly from bulk metal for efficient CO_2 reduction, Joule 3 (2019) 584–594.

[36] Q. Fan, C. Choi, C. Yan, Y. Liu, J. Qiu, S. Hong, Y. Jung, Z. Sun, High-yield production of few-layer boron nanosheets for efficient electrocatalytic N_2 reduction, Chem. Commun. 55 (2019) 4246–4249.

[37] Y.X. Duan, K.H. Liu, Q. Zhang, J.M. Yan, Q. Jiang, Efficient CO_2 reduction to HCOOH with high selectivity and energy efficiency over Bi/rGO catalyst, Small Methods 4 (2020) 1900846.

[38] H. Tao, Q. Fan, T. Ma, S. Liu, H. Gysling, J. Texter, F. Guo, Z. Sun, Two-dimensional materials for energy conversion and storage, Prog. Mater. Sci. 111 (2020) 100637.

[39] C. Xia, P. Zhu, Q. Jiang, Y. Pan, W. Liang, E. Stavitsk, H.N. Alshareef, H. Wang, Continuous production of pure liquid fuel solutions via electrocatalytic CO_2 reduction using solid-electrolyte devices, Nat. Energy 4 (2019) 776.

[40] Q. Gong, P. Ding, M. Xu, X. Zhu, M. Wang, J. Deng, Q. Ma, N. Han, Y. Zhu, J. Lu, Z. Feng, Y. Li, W. Zhou, Y. Li, Structural defects on converted bismuth oxide nanotubes enable highly active electrocatalysis of carbon dioxide reduction, Nat. Commun. 10 (2019) 2807.

[41] Y. Zhang, F. Li, X. Zhang, T. Williams, C.D. Easton, A.M. Bond, J. Zhang, Electrochemical reduction of CO_2 on defect-rich Bi derived from Bi_2S_3 with enhanced formate selectivity, J. Mater. Chem. A 6 (2018) 4714–4720.

[42] F.P.G. de Arquer, O.S. Bushuyev, P.D. Luna, C.T. Dinh, A. Seifitokaldani, M.I. Saidaminov, C.S. Tan, L.N. Quan, A. Proppe, M.G. Kibria, S.O. Kelley, D. Sinton, E.H. Sargent, 2D metal oxyhalide-derived catalysts for efficient CO_2 electroreduction, Adv. Mater. 30 (2018) 1802858.